

Article

Seven-Rod Pumping Concept for Highly Stable Solar Laser Emission

Hugo Costa, Dawei Liang ^{*}, Joana Almeida, Miguel Catela, Dário Garcia, Bruno D. Tibúrcio and Cláudia R. Vistas

Centre of Physics and Technological Research, Physics Department, NOVA School of Science and Technology, 2829-516 Caparica, Portugal

* Correspondence: dl@fct.unl.pt

Abstract: A seven-rod solar laser head was conceptualized and numerically studied to improve the tracking error compensation capacity and power stability in end-side-pumping schemes. It was composed of a first-stage heliostat–parabolic mirror system, a second-stage fused silica aspheric lens and a third-stage conical pumping cavity, within which seven Nd:YAG rods were mounted. Highly stable solar laser emission, with a power loss inferior to 5% for tracking errors up to $\pm 0.4^\circ$, could potentially be enabled with seven 4 mm diameter, 13 mm length rods. The tracking error width at 10% laser power loss was about 1.0° , which is 1.65 times higher than the experimental record, attained by a dual-rod side-pumping prototype. Furthermore, a total multimode laser power of about 41.2 W could also be achieved, corresponding to 23.3 W/m² collection and 2.5% solar-to-laser power conversion efficiencies, which are 1.65 and 1.36 times higher than those obtained with the dual-rod side-pumping prototype. They are also 1.27 and 1.12 times higher than the multirod experimental records in multimode regime for the same rod material.

Keywords: multirod; Nd:YAG; solar concentration; solar laser; tracking error compensation capacity



Citation: Costa, H.; Liang, D.; Almeida, J.; Catela, M.; Garcia, D.; Tibúrcio, B.D.; Vistas, C.R. Seven-Rod Pumping Concept for Highly Stable Solar Laser Emission. *Energies* **2022**, *15*, 9140. <https://doi.org/10.3390/en15239140>

Academic Editor: Tapas Mallick

Received: 28 October 2022

Accepted: 30 November 2022

Published: 2 December 2022

Publisher's Note: MDPI stays neutral with regard to jurisdictional claims in published maps and institutional affiliations.



Copyright: © 2022 by the authors. Licensee MDPI, Basel, Switzerland. This article is an open access article distributed under the terms and conditions of the Creative Commons Attribution (CC BY) license (<https://creativecommons.org/licenses/by/4.0/>).

1. Introduction

Solar energy can be used for direct and indirect pumping of solid-state lasers. In indirect pumping, solar cells convert sunlight into electricity to power diode lasers, which will then emit a beam that pumps the solid-state laser. In contrast, directly converting the natural sunlight into narrowband, collimated laser radiation skips two energy conversion stages, potentially leading to higher efficiency, simplicity, and reliability. For these reasons, solar-pumped laser systems are considered an emerging technology for both renewable energy and laser-based research, despite being much less mature. Not only can they be used in fields such as materials processing [1], but space-based applications have also been proposed, including wireless power transmission [2], deep-space optical data transmission and networking [3], laser propulsion [4], and asteroid deflection [5].

The first solar-pumped laser emission was reported by Kiss et al., in 1963, involving the usage of a CaF₂:Dy²⁺ system [6]. Three years later, Young obtained a 1 W laser output from a Nd:YAG rod [7]. This material has been the most commonly used for solar pumping and has proven to be quite effective in producing solar laser as a result of its availability, reasonably low cost, good thermomechanical properties [8], and the spectroscopic properties of the dopant [9]. Initially, the main focus was to produce as much laser power as possible, with Arashi et al. establishing a record value of 18 W [10] and then Weksler and Shwartz surpassing it with a 60 W solar laser emission [8], both achieved in the 1980s. However, with the turn of the century, the primary concentration area started to be taken into consideration when evaluating the system's performance and high collection efficiency became the most desirable goal [11–19]. The solar-to-laser power conversion efficiency is another important parameter that researchers have been mindful of. It can be defined as the ratio between

the laser power generated and the total input solar pump power and does not depend on the solar irradiance, unlike the collection efficiency. The record values for both of these figures of merit with a single rod were established in 2022, with Garcia et al. reaching a 38.2 W/m^2 collection efficiency and a 4.5% solar-to-laser power conversion efficiency by end-side-pumping a 2.5 mm diameter, 25 mm length Ce:Nd:YAG rod [19].

From heavy industry to consumer electronics, lasers are seen as a vital tool for materials processing. In search for productivity enhancement, manufacturers started to deploy several laser beams on the same workpiece, with each performing a part of the overall procedure, which has led to superior results that are unachievable with a singular laser beam [20]. Moreover, in the classical single-thick-rod solar-pumped laser systems, thermal lens and thermal stress problems have always been present. In that regard, solar-pumped laser systems with multiple rods have been both numerically and experimentally studied to understand their potential in terms of performance [21–34], with researchers also looking to circumvent hindrances, such as laser beam distortion and rod fracture, by evenly dividing the total amount of concentrated solar radiation between the rods. The first emission of three concurrent continuous-wave solar laser beams was reported in 2020, through three 3 mm diameter, 25 mm length Nd:YAG rods in an end-side-pumping configuration within a single conical pump cavity [25]. They produced a total of 18.30 W multimode laser power, which corresponded to 18.3 W/m^2 collection efficiency and 2.2% solar-to-laser power conversion efficiency. In 2022, a dual-rod system, in which two Nd:YAG rods with 4 mm diameter and different lengths (35 mm and 30 mm) were side-pumped, reportedly produced 14.81 W total laser power [33]. This corresponded to 14.1 W/m^2 collection and 1.8% conversion efficiencies. In the same year, an end-side-pumping system with three 2.5 mm diameter, 25 mm length Ce:Nd:YAG rods inside a single conical pump cavity produced 16.50 W total multimode laser power, corresponding to a 41.3 W/m^2 collection efficiency and a 4.6% solar-to-laser power conversion efficiency [34]. In these three systems, substantial amelioration of the thermal performance of the rods was also achieved.

Solar tracking systems perform a pivotal part in the progress of solar concentration applications [35] and, since their first introduction in 1962, have been investigated in an effort to improve the collection efficiency of concentration systems [36,37]. Some may offer simplicity in the way they operate, without using mechanical components or sensing units that assist them in tracking the Sun [38]; however, they lack accuracy and energy gain in comparison to the more intricate systems [39]. Currently, tracking systems can be mainly classified by two types based on movement capability: single-axis or two-axis [40]. Solar concentrator technologies, such as parabolic concentrators, require two-axis tracking systems [35].

Solar tracking error is an important issue that should not be overlooked when designing a solar-pumped laser system. Any slight deviation from optimal alignment during experimental testing can prevent the stable emission of laser, possibly leading to a severe depletion of the output power. This was experimentally investigated through the above-mentioned dual-rod side-pumping system [33]. For a solar tracking error of $\pm 0.5^\circ$ in the x -axis (azimuth) and y -axis (altitude), the laser power decreased 15.04% and 6.60%, respectively (Figure 1). In end-side-pumping systems, the loss in laser power can be even more noticeable, considering it entails the direct focusing of the concentrated solar power onto the end face of the laser rod. Even though this problem can be attenuated by using a Fresnel lens since the solar-pumped laser system would be operated in direct solar tracking mode, the constant movement of the laser head fixed at the solar tracker throughout the day can constitute an inconvenience for many applications. Conversely, with a heliostat–parabolic mirror system, the laser head is fixed in a stationary position within the solar laser facility, which can be preferred.

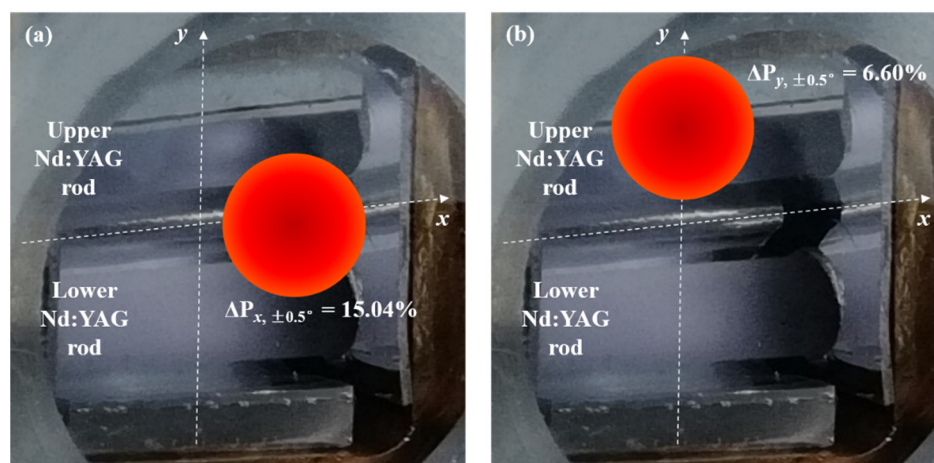


Figure 1. Photograph of the pump cavity with two Nd:YAG rods from the side-pumping prototype by Tibúrcio et al. [33]. ΔP is the variation of laser power observed when a deviation from optimal alignment occurs due to solar tracking error ($\pm 0.5^\circ$ in the (a) x - and (b) y -axes).

A seven-rod end-side-pumping solar laser concept is presented here. The collection and concentration of solar rays were performed by the heliostat–parabolic mirror system at the NOVA School of Science and Technology. A fused silica aspheric lens further concentrated the solar rays, which were then absorbed by seven Nd:YAG rods mounted inside a single conical pump cavity. The design parameters of this concept were numerically optimized by use of the Zemax[®] ray tracing in non-sequential mode and the LASCAD[™] software. By using seven 2.15 mm diameter, 17 mm length Nd:YAG rods, this scheme could enable the production of 50.30 W multimode laser power at optimal alignment, which corresponds to a 28.5 W/m² collection efficiency and a 3.0% solar-to-laser power conversion efficiency. More importantly, with seven 4.00 mm diameter, 13 mm length rods, high solar tracking compensation capacity and power stability were found, despite the lower total laser power of 41.16 W.

2. Description of the Seven-Rod Solar Laser Concept

2.1. NOVA Heliostat–Parabolic Mirror System

The solar facility at the NOVA School of Science and Technology has a collection and concentration system comprised of a two-axis heliostat as well as a motionless parabolic mirror (Figure 2). The heliostat, which incorporates a large plane two-segment mirror, tracks the Sun and reflects the solar rays towards the parabolic mirror with 1.5 m diameter, 60° rim angle and 0.66 m focal length. All the mirrors are back-surface silver-coated. The glass substrate of each flat segment of the heliostat is 4 mm thick with low iron content, allowing 93.5% of the incoming radiation to be reflected. On the other hand, the high iron content glass substrate with 10 mm thickness, the absence of antireflection coatings on its front surface, and long-time usage since the 1940s limited the parabolic mirror’s reflectivity to about 80%. In a clear sunny day with 950 W/m² solar irradiance, the collection and concentration system can focus about 1250 W of solar power into a highly concentrated pump light spot with a nearly Gaussian distribution and a full width at half maximum of 8 mm.

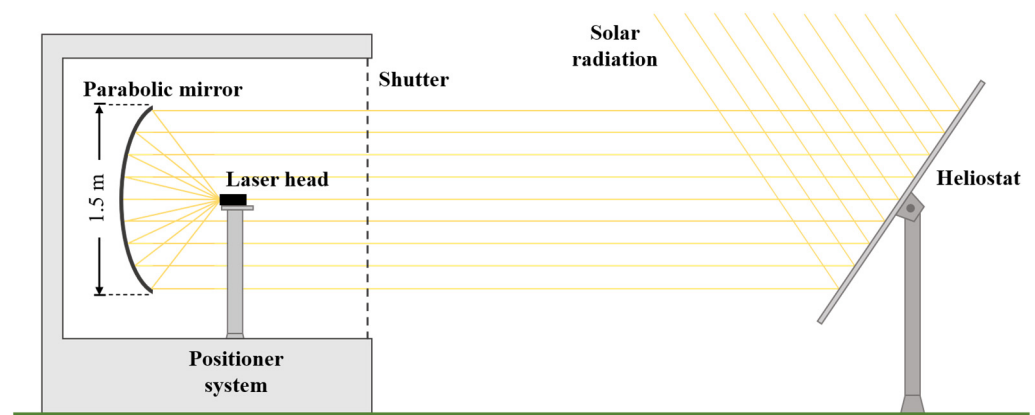


Figure 2. Schematic of the NOVA heliostat–parabolic mirror system.

2.2. Solar Laser Head Design for Highly Stable Laser Emission

The solar laser head (Figure 3) consisted of a fused silica aspheric lens and a conical pump cavity, inside of which seven Nd:YAG rods were mounted. The aspheric lens had an 82 mm diameter, a 37 mm height, and a -43 mm rear radius, and its plane output face coincided with the position of the parabolic mirror’s focal spot, further concentrating the solar radiation that came from the parabolic mirror (Figure 3a). Fused silica is a highly suitable optical material for systems with Nd:YAG rods, due to its transparency over the absorption spectrum of the Nd:YAG material and acting as a filter of radiation undesirable to the laser medium. Moreover, it has a low thermal expansion coefficient and high resistance to scratching and thermal shock [41].

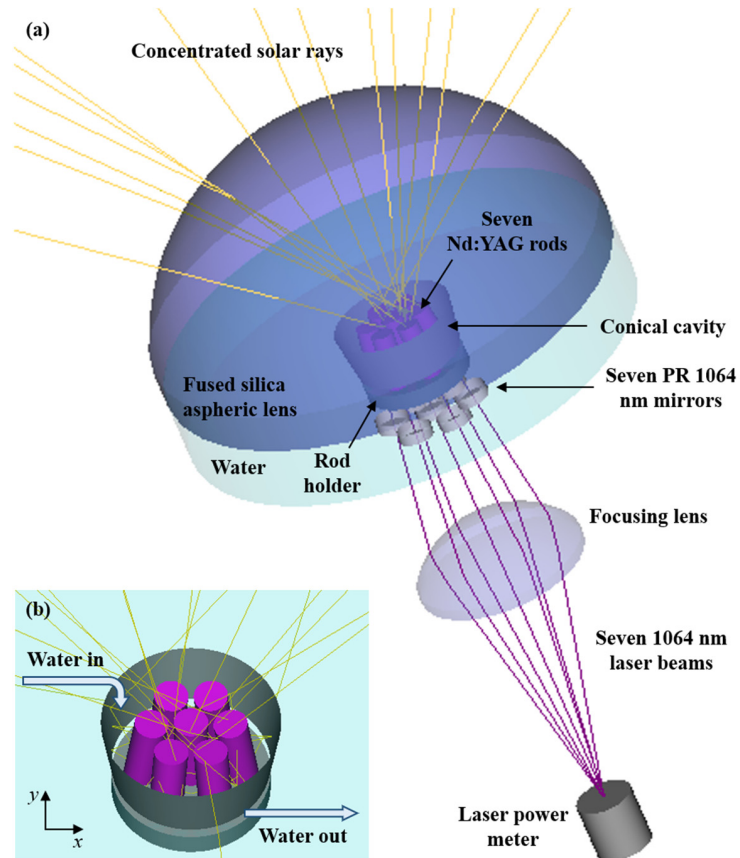


Figure 3. Three-dimensional view of (a) the solar laser head and (b) the conical pump cavity with seven Nd:YAG rods.

The hollow conical pump cavity, with 21.0 mm input diameter, 18.6 mm output diameter, and 8.5 mm length, was placed 1.5 mm below the output face of the aspheric lens. At 1.5 mm after the output end face of the pump cavity, a 3 mm thickness rod holder was utilized for mechanical fixing of the seven 4.00 mm diameter and 13 mm length Nd:YAG rods. As illustrated in Figure 3b, six external rods were tilted 7.5° in rotational symmetry in relation to the central rod to ensure compactness of the seven rods at the entrance of the conical cavity for efficient pump light coupling and sufficient space for the mechanical fixing of the laser rods, with the fixed end of the external rods being 2.3 mm away from that of the central one. The use of the conical pump cavity enabled zigzagging of the solar rays that were concentrated by the fused silica aspheric lens; with this, each solar ray could pass through multiple rods and be partially absorbed by each one. A 95% reflectivity was considered for both the conical pump cavity and the rod holder.

The cooling system was devised to mitigate the generation of heat within the rods and the optical components. Water entered through the input face of the conical cavity and left through its output face, being in direct contact with the plane output face of the fused silica aspheric lens and the seven Nd:YAG rods. Since the refractive index of water (≈ 1.33) is lower than the fused silica's (≈ 1.46), the rays were refracted towards the rods, enabling a more efficient concentration of the pump radiation. Due to it also being lower than the Nd:YAG's (≈ 1.82), a part of the concentrated radiation that is directly focused onto the top end face of the rods travelled within them through total internal reflection.

A coating of high reflectivity (HR) at 1064 nm (laser emission wavelength) was added to the top end face of each of the seven Nd:YAG rods, while the opposite end surface presented an antireflective (AR) at 1064 nm coating. The HR coating, the laser rod and an output mirror that is partially reflective (PR) at 1064 nm, through which a solar laser beam was emitted, formed each laser resonator.

The seven laser beams are produced simultaneously, diverging from each other. A focusing lens can be used to converge them towards a single laser power meter to verify the value of the total solar laser output power (Figure 3a). These seven laser beams can also be used separately through optical fiber coupling techniques, for example, for different applications.

3. Numerical Modeling of the Seven-Rod Solar Laser Concept

3.1. Modeling of the Design Parameters through Zemax[®]

Before the design parameters of the solar laser head were optimized in Zemax[®], other parameters had to be defined. The terrestrial solar irradiance of 950 W/m^2 and the 16% overlap between the absorption spectrum of the Nd:YAG material and the solar spectrum [19] were considered in the calculation of the effective pump power of the light source. After consulting the direct standard solar spectrum for one-and-a-half air mass [42], 22 spectral irradiance values at the peak absorption wavelengths for the 1.0 at.% Nd:YAG material were included as reference data for the light source. The absorption coefficient for each of those wavelengths [43] was used in the glass catalog data for Nd:YAG. To account for the absorption losses in fused silica and water, the absorption spectra and wavelength-dependent refractive indices of those materials [19] were also added to the glass catalog data.

To examine the numerical information within each rod, the use of a detector volume was required. The absorbed pump power in each rod was calculated by summing up the power in each of the voxels that the detector volume was comprised of. By using 4×10^6 analysis rays and detector volumes with 50,000 voxels, accurate results and good image resolution in each detector were possible. The absorbed pump flux distribution in the longitudinal and five transversal cross-sections of the central and one external Nd:YAG rods is shown in Figure 4. It is worth mentioning that, in view of the six external rods showing identical absorbed pump profiles with rotational symmetry around the central point of the pump cavity, only one of those was presented. The maximum pump flux is

represented in red color, while blue is used to represent areas of the rods where there is little absorption or none.

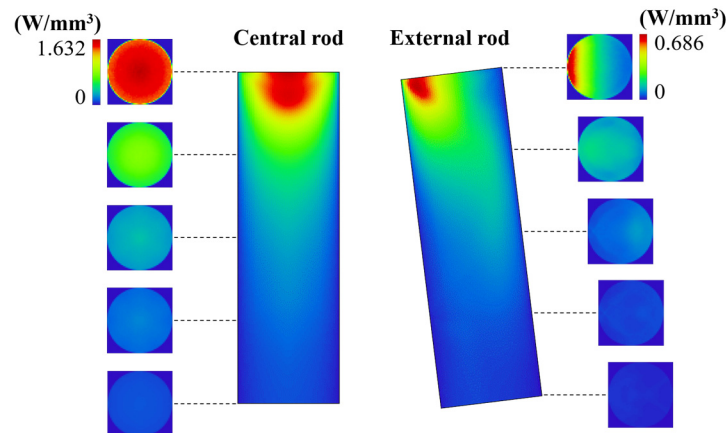


Figure 4. Absorbed pump flux distribution in the longitudinal and five transversal cross-sections of the central and one external Nd:YAG rods, with 4.00 mm diameter and 13 mm length.

After each simulation, the absorbed pump flux data was exported from Zemax[®] and imported into the LASCAD[™] software, to compute the thermal effects applied to each active media and to find the highest solar laser output power provided by the optimal resonator beam parameters. Based on these results, the design parameters were further optimized in Zemax[®].

3.2. Modeling of the Laser Resonator Parameters through LASCAD[™]

One of the most important parameters to calculate the laser output power is the pump rate W_p , which is defined by the equation [44]:

$$W_p = \frac{4C}{N_t D} \int_{520 \text{ nm}}^{880 \text{ nm}} \eta_T(\lambda) \frac{I(\lambda)}{h \nu_p(\lambda)} \eta_U(\lambda) [1 - e^{-\alpha(\lambda)l}] d\lambda. \quad (1)$$

Here, C is the concentration factor of the collection and concentration system, N_t the total number density of the active ions in the laser rod with diameter D , $\eta_T(\lambda)$ the solar power transfer efficiency from the primary solar collector to the surface of the rod, $I(\lambda)$ the one-sun solar spectral irradiance, h the Planck constant, $\nu_p(\lambda)$ the pump frequency, η_U the upper state efficiency, $\alpha(\lambda)$ the absorption coefficient of the laser medium, and l the effective absorption length. The integration is performed only over the laser absorption bands, as indicated by the $\lambda = 520 \text{ nm}$ and $\lambda = 880 \text{ nm}$. For the LASCAD[™] software to determine W_p , only the mean absorbed and intensity-weighted solar pump wavelength λ_p is required. From the equation [8]:

$$\lambda_p = \frac{\int_{520 \text{ nm}}^{880 \text{ nm}} I(\lambda) \lambda d\lambda}{\int_{520 \text{ nm}}^{880 \text{ nm}} I(\lambda) d\lambda}, \quad (2)$$

$\lambda_p = 660 \text{ nm}$ can be calculated. A stimulated emission cross-section of $2.8 \times 10^{-19} \text{ cm}^2$, a fluorescence lifetime of $230 \mu\text{s}$ [45], and a typical absorption and scattering loss of 0.002 cm^{-1} for the 1.0 at.% Nd:YAG medium were also considered in the LASCAD[™] analysis.

In this software, as displayed in Figure 5, each of the seven laser resonators was composed of two opposing mirrors, which represent the HR 1064 nm coating (99.98% reflectivity) and the PR 1064 nm output mirror (reflectivity varying between 90% and 99%), whose optical axes were in alignment with that of the Nd:YAG rod. A 5 mm separation length between the rightmost end face of each rod and the PR 1064 nm output mirror was adopted for the extraction of maximum laser beam power in multimode regime.

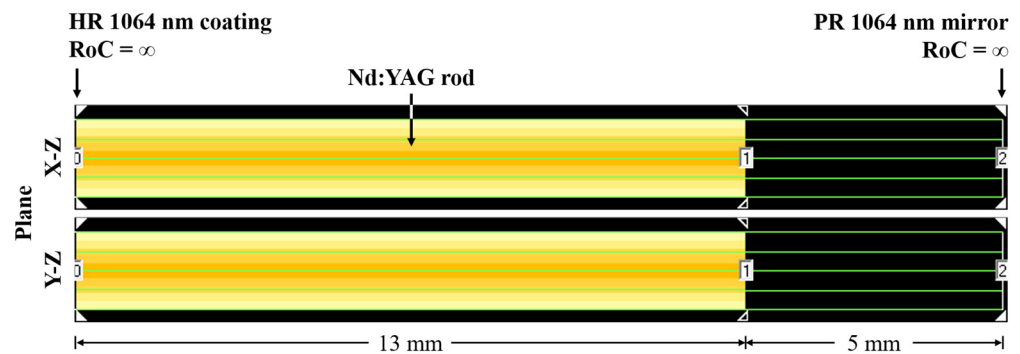


Figure 5. Laser resonator design in LASCAD™ for one 4.00 mm diameter, 13 mm length Nd:YAG rod. RoC is the radius of curvature.

4. Numerical Analysis of the Seven-Rod Solar Laser Concept

4.1. Solar Laser Performance in Multimode Regime

To estimate the maximum multimode laser power that the seven-rod concept could produce, different rod lengths (L) were tested for each rod diameter (D), while optimizing the design parameters of the other components. The fused silica aspheric lens described in Section 2.2 was used during the entirety of this process, as it always led to the best results.

As shown in Figure 6, the highest total laser power of 50.30 W was achieved using seven $D = 2.15$ mm, $L = 17$ mm rods, with 12.92 W from the central rod and 6.23 W from each of the six external ones. This corresponds to a collection efficiency of 28.5 W/m^2 and a solar-to-laser power conversion efficiency of 3.0%. For this case, the conical pump cavity had a 19.0 mm input diameter, a 13.5 mm output diameter, and a 12.5 mm length, while the six external rods had their fixed end 2.55 mm away from the central rod's.

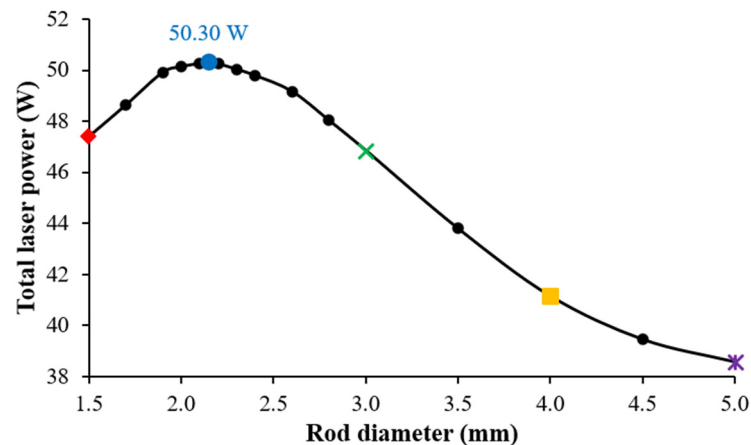


Figure 6. Total laser power in multimode regime as a function of rod diameter. Five configurations were selected to study tracking error compensation capacity and power stability: $D = 1.5$ mm, $D = 2.15$ mm, $D = 3.0$ mm, $D = 4.0$ mm, and $D = 5.0$ mm.

4.2. Tracking Error Compensation Capacity and Power Stability

To study the tracking error compensation capacity and power stability of the seven-rod ($N = 7$) concept, five of the configurations previously tested were selected: $D = 1.5$ mm, $D = 2.15$ mm, $D = 3.0$ mm, $D = 4.0$ mm, and $D = 5.0$ mm. Due to the heliostat's reflecting area being much larger than that of the parabolic mirror, no loss of absolute irradiated area of the latter is verified. Therefore, only angular variation was considered. Typical solar tracking error up to $\pm 0.5^\circ$ in the x - and y -axes was numerically investigated. A similar scheme with a single Nd:YAG rod ($N = 1$) was also optimized in order to compare results. A $D = 5.70$ mm, $L = 19$ mm rod provided the highest multimode laser power (55.51 W), using a conical pump cavity with 15.0 mm input diameter, 8.4 mm output diameter, and

14.5 mm length. Figure 7 shows the total multimode laser power as a function of the tracking error for each of the six aforementioned cases, while the tracking error width at 10% laser power loss ($TEW_{10\%}$) and the ΔP at different tracking errors are presented in Table 1 to facilitate the assessment of the tracking error compensation capacity and power stability, respectively, of each case.

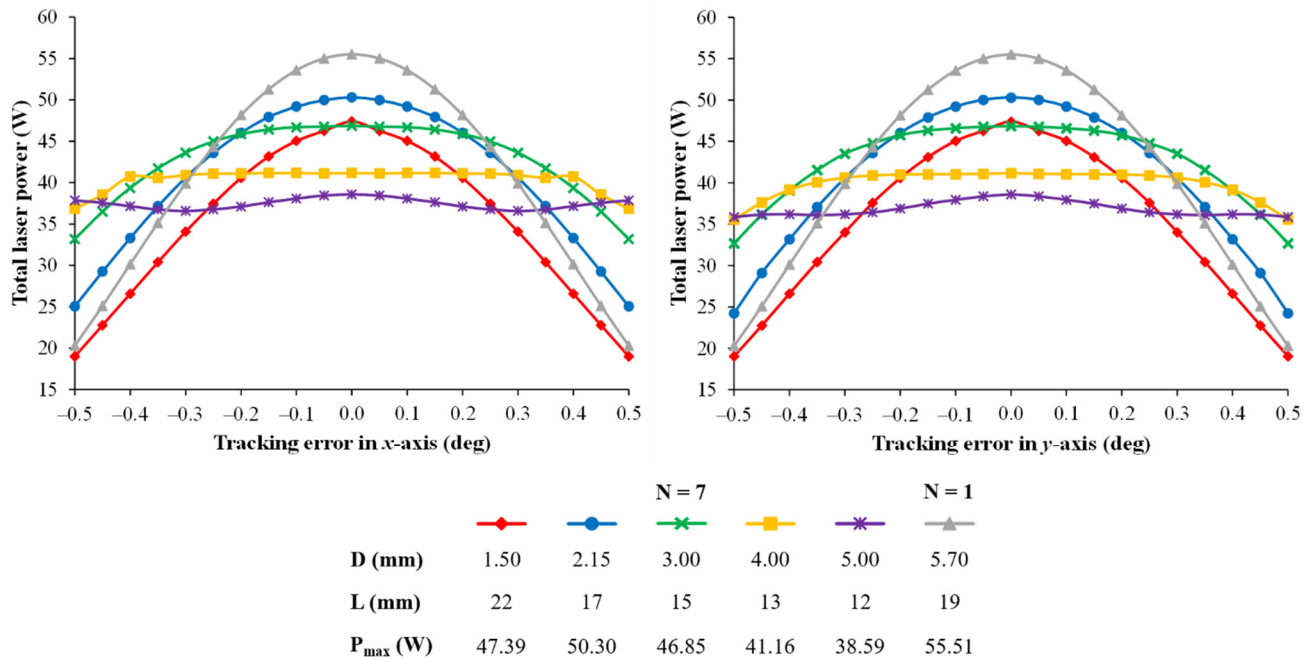


Figure 7. Total laser power in multimode regime as a function of the solar tracking error in the x - and y -axes, for different schemes tested. P_{max} is the maximum total laser power achieved at optimal alignment by each of the schemes presented.

Table 1. Tracking error width at 10% laser power loss ($TEW_{10\%}$) and ΔP at different solar tracking errors in the x - and y -axes, for different schemes tested.

		N = 7						N = 1					
D (mm)		1.50		2.15		3.00		4.00		5.00		5.70	
Axis		x	y	x	y	x	y	x	y	x	y	x	y
$TEW_{10\%}$ (deg)		0.32	0.32	0.43	0.43	0.68	0.67	0.99	0.93	—	—	0.34	
ΔP (%)	$\pm 0.1^\circ$	4.96	4.92	2.21	2.15	0.35	0.56	0.12	0.29	1.32	1.66	3.46	
	$\pm 0.2^\circ$	14.39	14.37	8.49	8.47	2.12	2.34	0.17	0.41	3.84	4.41	13.24	
	$\pm 0.3^\circ$	28.09	28.21	19.26	19.34	6.92	7.12	0.63	1.34	5.21	6.17	28.12	
	$\pm 0.4^\circ$	43.93	43.85	33.78	34.04	15.99	16.57	1.46	4.86	5.21	6.48	45.70	
	$\pm 0.5^\circ$	59.91	59.82	50.20	51.81	29.18	30.23	10.49	13.63	5.21	7.05	63.45	

The worst compensation capacity was found with the $N = 7$, $D = 1.50$ mm, $L = 22$ mm scheme ($TEW_{10\%} = 0.32^\circ$ in both axes), while the $N = 1$, $D = 5.70$ mm, $L = 19$ mm scheme, the one that produced the highest multimode laser power of 55.51 W, showed a marginally better compensation capacity ($TEW_{10\%} = 0.34^\circ$). Conversely, the schemes with seven rods of larger diameter displayed a better compensation capacity, with the $D = 5.00$ mm, $L = 12$ mm scheme being the only one with which a 10% power loss was not verified for a tracking error of $\pm 0.5^\circ$; however, in this case, the laser power slightly oscillated with the tracking error, making it not the most feasible. The most stable scheme was the $D = 4.00$ mm, $L = 13$ mm, with a power loss of 5% only being observed after the tracking error reached $\pm 0.4^\circ$. It is worth noting that, because of the six rods tilted in rotational

symmetry in relation to the central rod, with all of them being end-side-pumped, the tracking error compensation capacity and power stability in both x - and y -axes were nearly the same.

Figures 8–10 show 3D plots and heatmaps illustrating the total multimode laser power as a function of the tracking error for three of the configurations tested: $N = 1, D = 5.70$ mm, $L = 19$ mm; $N = 7, D = 2.15$ mm, $L = 17$ mm; and $N = 7, D = 4.00$ mm, $L = 13$ mm, respectively. The $N = 1, D = 5.70$ mm, $L = 19$ mm scheme exhibits a considerable decrease of the laser power with the increase of the tracking error, attributable to the direct focusing of the concentrated solar power onto the end face of a single rod. By placing six rods around a central one, for the $N = 7$ schemes, that reduction was attenuated because the seven rods ended up occupying a larger area and the concentrated solar power was harnessed more efficiently. This was especially evident for the $D = 4.00$ mm scheme owing to the use of larger diameter rods, leading to highly stable laser emission even when the tracking error was relatively high.

$N = 1, D = 5.70$ mm, $L = 19$ mm

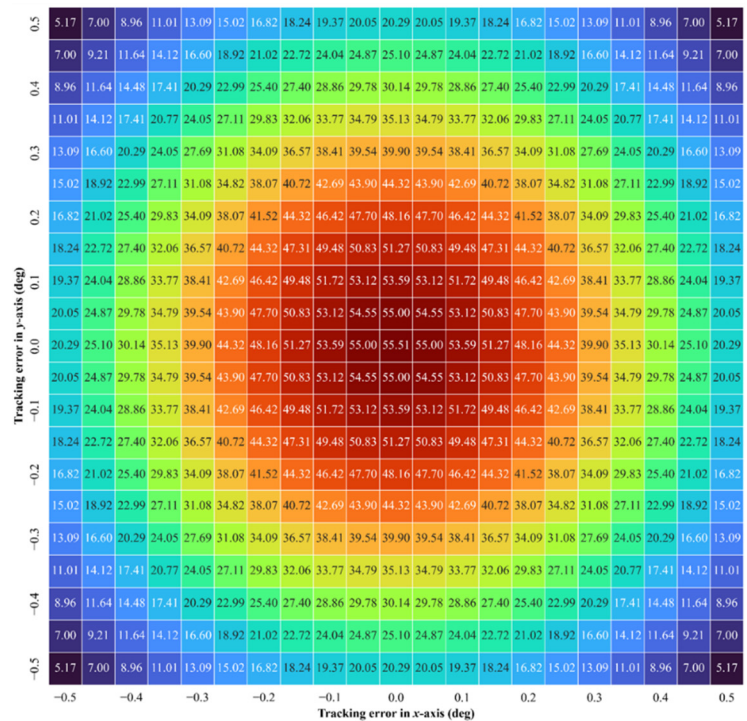
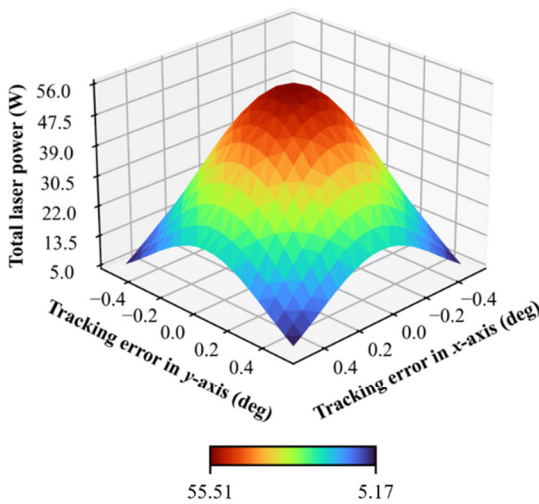


Figure 8. Total solar laser power in multimode regime as a function of the solar tracking error for the single 5.70 mm diameter, 19 mm length rod scheme.

$N = 7, D = 2.15 \text{ mm}, L = 17 \text{ mm}$

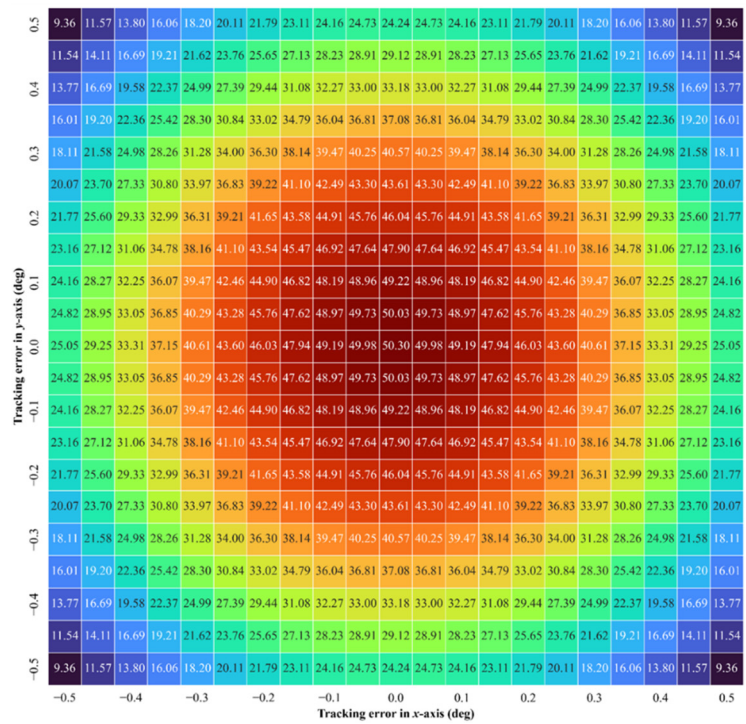
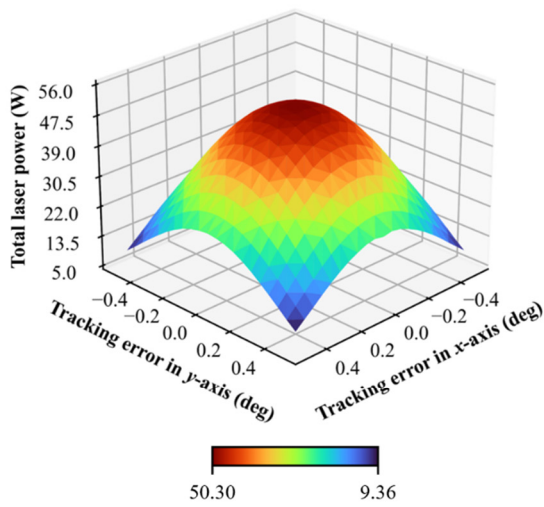


Figure 9. Total solar laser power in multimode regime as a function of the solar tracking error for the seven 2.15 mm diameter, 17 mm length rods scheme.

$N = 7, D = 4.00 \text{ mm}, L = 13 \text{ mm}$

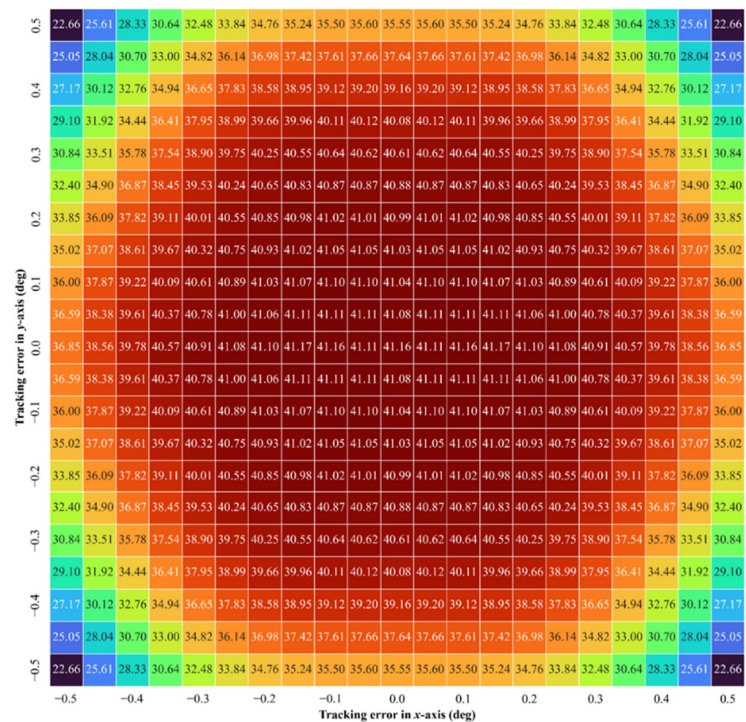
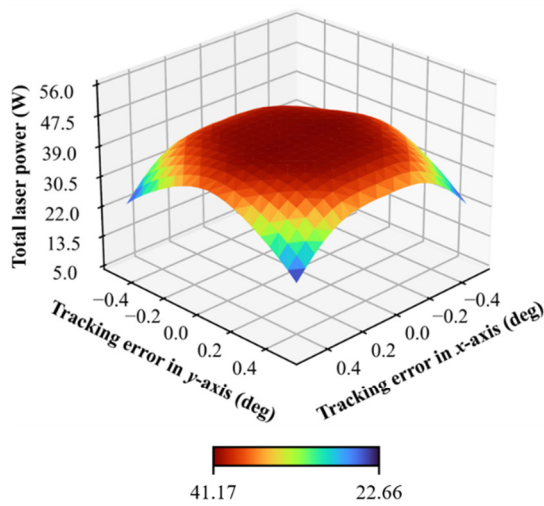


Figure 10. Total solar laser power in multimode regime as a function of the solar tracking error for the seven 4.00 mm diameter, 13 mm length rods scheme.

4.3. Thermal Performance

In Figure 11, the thermally induced effects (heat load, temperature, and stress intensity), in the case of optimal alignment, are illustrated for the central and one external

Nd:YAG rods from three of the configurations tested: $N = 1$, $D = 5.70$ mm, $L = 19$ mm; $N = 7$, $D = 2.15$ mm, $L = 17$ mm; and $N = 7$, $D = 4.00$ mm, $L = 13$ mm.

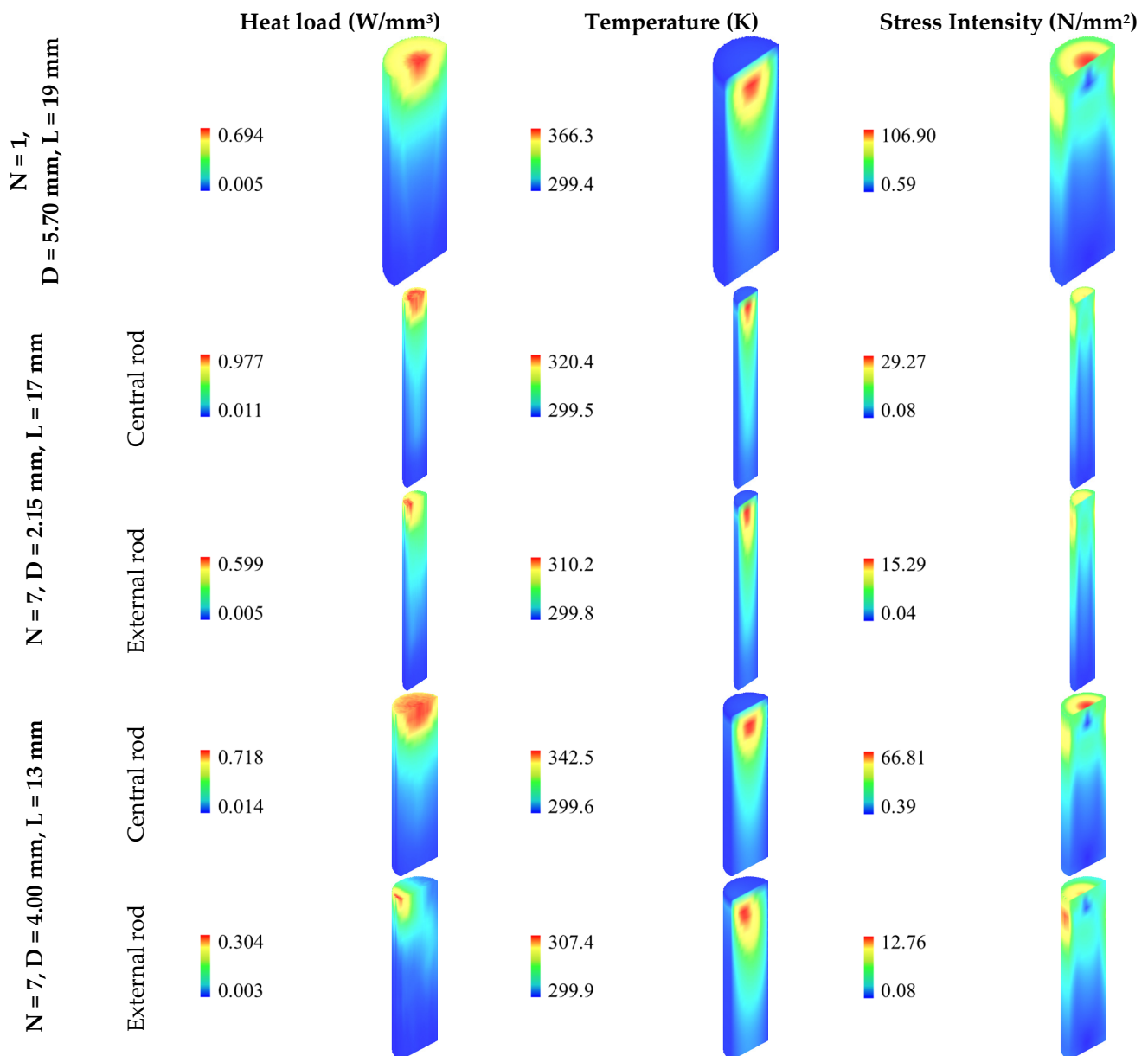


Figure 11. Heat load, temperature and stress intensity for the central and one external Nd:YAG rods from three of the schemes tested: $N = 1$, $D = 5.70$ mm, $L = 19$ mm; $N = 7$, $D = 2.15$ mm, $L = 17$ mm; and $N = 7$, $D = 4.00$ mm, $L = 13$ mm.

Out of the rods placed at the center of the conical pump cavity from each of the three cases, the one from the $N = 7$, $D = 2.15$ mm, $L = 17$ mm scheme was where the heat load was more pronounced (0.977 W/mm³), while the rod from the $N = 1$, $D = 5.70$ mm, $L = 19$ mm scheme reached the highest temperature (366.3 K). In regard to the stress intensity, the highest registered value was 106.90 N/mm² with the $N = 1$, $D = 5.70$ mm, $L = 19$ mm scheme, which is slightly more than half of the Nd:YAG material's stress fracture limit (200.0 N/mm² [46]). In contrast, with seven rods, the highest value of only 66.81 N/mm² was obtained in the central rod of the $N = 7$, $D = 4.00$ mm, $L = 13$ mm scheme, corresponding to around a third of that limit. In the external rods of the $N = 7$ schemes, the thermally induced effects were more noticeable in the $D = 2.15$ mm, $L = 17$ mm scheme, as expected in the case of optimal alignment, as a result of the placement of the thinner laser

rods nearer the center of the conical pump cavity. Nevertheless, all rods would perform relatively well under solar pumping of high intensity.

5. Discussion

The proposed seven-rod solar pumping scheme resulted in significant enhancements in comparison with other numerical works that included multiple Nd:YAG rods: the $D = 2.15$ mm, $L = 17$ mm in terms of efficiency, and the $D = 4.00$ mm, $L = 13$ mm pertaining to tracking error compensation capacity and power stability. Table 2 summarizes the results of the present work and those from four other numerical studies that our research group has conducted: a dual-rod scheme by Tibúrcio et al. [24], a four-rod scheme by Catela et al. [47], and seven-rod schemes by Almeida et al. [27] and Liang et al. [29].

Table 2. Comparison between the results in multimode regime of the present work and the ones from the numerical works by Tibúrcio et al. [24], Catela et al. [47], Almeida et al. [27], and Liang et al. [29].

Parameter		Tibúrcio et al. (2020) [24]	Catela et al. (2022) [47]	Almeida et al. (2020) [27]	Liang et al. (2021) [29]	Present Work	
						D = 2.15 mm L = 17 mm	D = 4.00 mm L = 13 mm
Primary concentrator		Parabolic mirror	Parabolic mirror	Parabolic mirror	Fresnel lens	Parabolic mirror	
Number of rods		2	4	7	7	7	
Configuration		Side-pumping	End-side-pumping	End-side-pumping	End-side-pumping	End-side-pump	
Effective collection area (m ²)		1.560	1.767	1.767	4.000	1.767	
Solar irradiance (W/m ²)		890	950	950	950	950	
Total laser power (W)		37.72	43.69	32.18	107.00	50.30	41.16
Collection efficiency (W/m ²)		24.2	24.7	18.2	26.8	28.5	23.3
Conversion efficiency (%)		2.9	2.6	1.9	2.8	3.0	2.5
TEW _{10%} (deg)	<i>x</i> -axis	0.70	0.76	—	—	0.43	0.99
	<i>y</i> -axis	0.50				0.43	0.93
$\Delta P_{\pm 0.1^\circ}$ (%)	<i>x</i> -axis	0.40	0.05	—	—	2.21	0.12
	<i>y</i> -axis	1.34				2.15	0.29
$\Delta P_{\pm 0.2^\circ}$ (%)	<i>x</i> -axis	2.41	0.43	—	—	8.49	0.17
	<i>y</i> -axis	7.29				8.47	0.41
$\Delta P_{\pm 0.3^\circ}$ (%)	<i>x</i> -axis	6.58	4.18	—	—	19.26	0.63
	<i>y</i> -axis	18.38				19.34	1.34
$\Delta P_{\pm 0.4^\circ}$ (%)	<i>x</i> -axis	—	13.85	—	—	33.78	1.46
	<i>y</i> -axis	—				34.04	4.86
$\Delta P_{\pm 0.5^\circ}$ (%)	<i>x</i> -axis	—	29.77	—	—	50.20	10.49
	<i>y</i> -axis	—				51.81	13.63

Compared to these other proposed seven-rod solar laser concepts, the $D = 2.15$ mm, $L = 17$ mm scheme of the present work was more efficient, with 28.5 W/m² collection and 3.0% solar-to-laser power conversion efficiencies. These values represented improvements of 1.06 and 1.07 times, respectively, in relation to those from the seven-rod concept by Liang et al. [29], in which a Fresnel lens was employed as the primary concentrator. Moreover, the collection and conversion efficiencies were, respectively, 1.57 and 1.58 times higher than those from the scheme by Almeida et al. [27], for which the same collection and concentration system was employed. With the placement of each of the seven Nd:YAG rods in different pump cavities, each solar ray ended up not being shared by multiple rods in that scheme [27], resulting in this difference in efficiency.

Out of the four abovementioned numerical studies, the influence of the tracking error on the total laser power was examined in only two. The seven $D = 4.00$ mm, $L = 13$ mm rod scheme had better tracking error compensation capacity and power stability than the dual-rod side-pump concept by Tibúrcio et al. [24]. The TEW_{10%} in the *x*- and *y*-axes were 1.41 and 1.86 times higher, and did not display a ΔP asymmetry in both axes as clearly, which is a result of the chosen pumping configuration. In comparison with the most stable four-rod scheme by Catela et al. (with $D = 4.55$ mm, $L = 15$ mm rods) [47], overall

improvements were also attained by the seven-rod approach. The $TEW_{10\%}$ in the x - and y -axes were 1.30 and 1.22 times higher, and the ΔP for tracking errors up to $\pm 0.5^\circ$ denote a better power stability. Even though the total laser power is 6% lower than that by the four-rod scheme, the seven-rod concept with a smaller rod diameter is much more suitable for future adoption of Ce:Nd:YAG rods to further boost the laser power [48], consequently reducing the risk of thermal fracture of the rods.

Because of the feasibility exhibited by the $D = 4.00$ mm, $L = 13$ mm scheme according to the numerical analysis, as a result of its tracking error compensation capacity and power stability, its results were compared to those from the experimental works by Liang et al. [25] and Tibúrcio et al. [33] (Table 3), both of which utilized multiple Nd:YAG rods and the collection and concentration system at the NOVA School of Science and Technology. The collection and solar-to-laser power conversion efficiencies achieved by the present numerical work constituted enhancements of 1.27 and 1.12 times in relation to those from the triple-rod end-side-pumping prototype by Liang et al. [25]. In comparison with the results from the dual-rod side-pumping system by Tibúrcio et al. [33], the collection and conversion efficiencies were 1.65 and 1.36 times higher. More importantly, however, is the difference in tracking error compensation capacity and power stability, since Tibúrcio et al. attained very distinct results for both axes. In the x -axis, the $TEW_{10\%}$ was 1.65 times higher, whereas it was 0.66 times lower in the y -axis. Analogously, the ΔP values were always better until a solar tracking error of $\pm 0.5^\circ$, where it was 1.43 times better in the x -axis but 0.48 times worse in the y -axis.

Table 3. Comparison between the results in multimode regime of the present work and the ones from the experimental works by Tibúrcio et al. [33], and Liang et al. [25].

Parameter	Experimental Work		Present Numerical Work	Improvement in Relation to (Times)	
	Tibúrcio et al. (2022) [33]	Liang et al. (2020) [25]	D = 4.00 mm L = 13 mm	Tibúrcio et al. (2022) [33]	Liang et al. (2020) [25]
Number of rods	2	3	7	—	—
Configuration	Side-pumping	End-side-pumping	End-side-pumping	—	—
Effective collection area (m ²)	1.050	1.000	1.767	—	—
Solar irradiance (W/m ²)	783	830	950	—	—
Total laser power (W)	14.81	18.30	41.16	—	—
Collection efficiency (W/m ²)	14.1	18.3	23.3	1.65	1.27
Conversion efficiency (%)	1.8	2.2	2.5	1.36	1.12
$TEW_{10\%}$ (deg)	x -axis	0.60	0.99	1.65	—
	y -axis	1.40	—	0.93	0.66
$\Delta P_{\pm 0.1^\circ}$ (%)	x -axis	3.40	0.12	28.33	—
	y -axis	1.22	—	0.29	4.21
$\Delta P_{\pm 0.2^\circ}$ (%)	x -axis	6.87	0.17	40.41	—
	y -axis	2.46	0.41	6.00	—
$\Delta P_{\pm 0.3^\circ}$ (%)	x -axis	9.80	0.63	15.56	—
	y -axis	3.79	1.34	2.83	—
$\Delta P_{\pm 0.4^\circ}$ (%)	x -axis	12.59	1.46	8.62	—
	y -axis	5.11	4.86	1.05	—
$\Delta P_{\pm 0.5^\circ}$ (%)	x -axis	15.04	10.49	1.43	—
	y -axis	6.60	13.63	0.48	—

6. Conclusions

A seven-rod solar laser concept was presented here to improve the tracking error compensation capacity and power stability in end-side-pumping schemes. It was composed of the first-stage heliostat–parabolic mirror system at the NOVA School of Science and

Technology, the second-stage fused silica aspheric lens, and the third-stage conical pumping cavity, inside of which seven Nd:YAG rods were mounted.

With seven 2.15 mm diameter, 17 mm length rods, the highest total multimode laser power of 50.30 W was attained, corresponding to 28.5 W/m² collection and 3.0% solar-to-laser power conversion efficiencies. These efficiency values represented enhancements of 1.06 and 1.07 times, respectively, in relation to those from the seven-rod end-side-pumping concept proposed by Liang et al., who employed a Fresnel lens as the primary concentrator [29], even with the use of the heliostat causing 6% more loss than with the direct solar tracking system. They were also, respectively, 1.57 and 1.58 times higher than those from another seven-rod end-side-pumping concept proposed for the same collection and concentration system as this work, in which each rod was mounted within a separate pump cavity [27].

The most feasible configuration of this scheme adopted seven 4.00 mm diameter, 13 mm length rods, due to the high tracking error compensation capacity and power stability being acquired. Overall, this configuration achieved better results than an experimental work by the same collection and concentration system, in which two Nd:YAG rods were side-pumped [33]. The TEW_{10%} was 1.65 times higher but 0.66 times lower in the *x*- and *y*-axes, respectively, and the ΔP values were mostly always better, with the exception being for a tracking error of $\pm 0.5^\circ$ in the *y*-axis, where the ΔP was 0.48 times worse. Furthermore, 41.16 W total multimode laser power was obtained, corresponding to 23.3 W/m² collection and 2.5% solar-to-laser power conversion efficiencies, which are, respectively, 1.65 and 1.36 times higher than those attained with the dual-rod side-pumping prototype [33]. They are also, respectively, 1.27 and 1.12 times higher than the multirod experimental records in multimode regime for the same rod material [25].

By taking the tracking error into consideration when designing a solar-pumped laser prototype, especially in an end-side-pumping configuration, the success of future experimental tests ends up not being so dependent on complex, expensive, and highly precise solar trackers, enabling the possibility to reduce the cost of the overall system. It is also worth noting that, when aiming for high tracking error compensation capacity and power stability in an end-side-pumping scheme, the maximum laser output power tends to be lower than the highest possible, owing to the use of rods with diameter larger than the optimal. Nevertheless, opting for Cr:Nd:YAG [18] and specially Ce:Nd:YAG [48] rods can be a solution to increase the laser power and efficiency, since the absorption spectra of these materials match better with the solar spectrum.

Author Contributions: Conceptualization, D.L., H.C. and J.A.; methodology, H.C., D.L., J.A. and C.R.V.; software, H.C., D.L., J.A., M.C. and D.G.; validation, H.C., D.L. and J.A.; formal analysis, H.C., D.L., J.A. and B.D.T.; investigation, H.C., J.A. and D.L.; resources, D.L. and J.A.; data curation, H.C., D.L. and J.A.; writing—original draft preparation, H.C.; writing—review and editing, H.C., D.L., J.A., M.C., D.G., B.D.T. and C.R.V.; visualization, H.C.; supervision, D.L. and J.A.; project administration, D.L.; funding acquisition, D.L. and J.A. All authors have read and agreed to the published version of the manuscript.

Funding: This research was funded by Fundação para a Ciência e a Tecnologia—Ministério da Ciência, Tecnologia e Ensino Superior (FCT-MCTES), grant number UIDB/00068/2020 and EXPL/FIS-OTI/0332/2021.

Data Availability Statement: Not applicable.

Acknowledgments: The FCT-MCTES fellowship grants 2021.06172.BD, CEECIND/03081/2017, SFRH/BD/145322/2019, PD/BD/142827/2018, PD/BD/128267/2016, and SFRH/BPD/125116/2016 for Hugo Costa, Joana Almeida, Miguel Catela, Dário Garcia, Bruno D. Tibúrcio, and Cláudia R. Vistas, respectively, are acknowledged.

Conflicts of Interest: The authors declare no conflict of interest. The funders had no role in the design of the study; in the collection, analyses, or interpretation of data; in the writing of the manuscript; or in the decision to publish the results.

References

1. Yabe, T.; Bagheri, B.; Ohkubo, T.; Uchida, S.; Yoshida, K.; Funatsu, T.; Oishi, T.; Daito, K.; Ishioka, M.; Yasunaga, N.; et al. 100 W-class solar pumped laser for sustainable magnesium-hydrogen energy cycle. *J. Appl. Phys.* **2008**, *104*, 083104. [[CrossRef](#)]
2. Lando, M.; Kagan, J.A.; Shimony, Y.; Kalisky, Y.Y.; Noter, Y.; Yogev, A.; Rotman, S.R.; Rosenwaks, S. Solar-pumped solid state laser program. *Int. Soc. Opt. Eng.* **1997**, *3110*, 196. [[CrossRef](#)]
3. Hemmati, H.; Biswas, A.; Djordjevic, I.B. Deep-Space Optical Communications: Future Perspectives and Applications. *Proc. IEEE* **2011**, *99*, 2020–2039. [[CrossRef](#)]
4. Rather, J.D.G.; Gerry, E.T.; Zeiders, G.W. *Investigation of Possibilities for Solar Powered High Energy Lasers in Space*; W. J. Schafer Associates, Inc.: Arlington, VA, USA, 1977.
5. Vasile, M.; Maddock, C.A. Design of a formation of solar pumped lasers for asteroid deflection. *Adv. Sp. Res.* **2012**, *50*, 891–905. [[CrossRef](#)]
6. Kiss, Z.J.; Lewis, H.R.; Duncan, R.C., Jr. Sun Pumped Continuous Optical Maser. *Appl. Phys. Lett.* **1963**, *2*, 93–94. [[CrossRef](#)]
7. Young, C.G. A Sun-Pumped cw One-Watt Laser. *Appl. Opt.* **1966**, *5*, 993. [[CrossRef](#)]
8. Weksler, M.; Shwartz, J. Solar-pumped solid-state lasers. *IEEE J. Quantum Electron.* **1988**, *24*, 1222–1228. [[CrossRef](#)]
9. Lupei, V.; Lupei, A.; Gheorghie, C.; Ikesue, A. Emission sensitization processes involving Nd³⁺ in YAG. *J. Lumin.* **2016**, *170*, 594–601. [[CrossRef](#)]
10. Arashi, H.; Oka, Y.; Sasahara, N.; Kaimai, A.; Ishigame, M. A Solar-Pumped cw 18 W Nd:YAG Laser. *Jpn. J. Appl. Phys.* **1984**, *23*, 1051–1053. [[CrossRef](#)]
11. Lando, M.; Kagan, J.; Linyekin, B.; Dobrusin, V. A solar-pumped Nd:YAG laser in the high collection efficiency regime. *Opt. Commun.* **2003**, *222*, 371–381. [[CrossRef](#)]
12. Yabe, T.; Ohkubo, T.; Uchida, S.; Yoshida, K.; Nakatsuka, M.; Funatsu, T.; Mabut, A.; Oyama, A.; Nakagawa, K.; Oishi, T.; et al. High-efficiency and economical solar-energy-pumped laser with Fresnel lens and chromium codoped laser medium. *Appl. Phys. Lett.* **2007**, *90*, 261120. [[CrossRef](#)]
13. Liang, D.; Almeida, J. Highly efficient solar-pumped Nd:YAG laser. *Opt. Express* **2011**, *19*, 26399. [[CrossRef](#)] [[PubMed](#)]
14. Dinh, T.H.; Ohkubo, T.; Yabe, T.; Kuboyama, H. 120 watt continuous wave solar-pumped laser with a liquid light-guide lens and an Nd:YAG rod. *Opt. Lett.* **2012**, *37*, 2670. [[CrossRef](#)] [[PubMed](#)]
15. Xu, P.; Yang, S.; Zhao, C.; Guan, Z.; Wang, H.; Zhang, Y.; Zhang, H.; He, T. High-efficiency solar-pumped laser with a grooved Nd:YAG rod. *Appl. Opt.* **2014**, *53*, 3941. [[CrossRef](#)] [[PubMed](#)]
16. Liang, D.; Almeida, J.; Vistas, C.R.; Guillot, E. Solar-pumped Nd:YAG laser with 31.5 W/m² multimode and 7.9 W/m² TEM₀₀-mode collection efficiencies. *Sol. Energy Mater. Sol. Cells* **2017**, *159*, 435–439. [[CrossRef](#)]
17. Guan, Z.; Zhao, C.; Li, J.; He, D.; Zhang, H. 32.1 W/m² continuous wave solar-pumped laser with a bonding Nd:YAG/YAG rod and a Fresnel lens. *Opt. Laser Technol.* **2018**, *107*, 158–161. [[CrossRef](#)]
18. Liang, D.; Vistas, C.R.; Tibúrcio, B.D.; Almeida, J. Solar-pumped Cr:Nd:YAG ceramic laser with 6.7% slope efficiency. *Sol. Energy Mater. Sol. Cells* **2018**, *185*, 75–79. [[CrossRef](#)]
19. Garcia, D.; Liang, D.; Vistas, C.R.; Costa, H.; Catela, M.; Tibúrcio, B.D.; Almeida, J. Ce:Nd:YAG Solar Laser with 4.5% Solar-to-Laser Conversion Efficiency. *Energies* **2022**, *15*, 5292. [[CrossRef](#)]
20. Strite, T.; Gusenko, A.; Grupp, M.; Hoult, T. Multiple Laser Beam Material Processing. *Biul. Inst. Spaw.* **2016**, *60*, 30–33. [[CrossRef](#)]
21. Fazilov, A.; Riskiev, T.T.; Abdurakhmanov, A.A.; Bakhranov, S.A.; Makhkamov, S.; Mansurov, M.M.; Mukhamediev, E.J.; Paiziev, S.D.; Klychev, S.I.; Saribaev, A.S.; et al. Concentrated solar energy conversion to powerful laser radiation on neodymium activated yttrium-aluminum garnet. *Appl. Sol. Energy* **2008**, *44*, 93–96. [[CrossRef](#)]
22. Almeida, J.; Liang, D.; Tibúrcio, B.D.; Garcia, D.; Vistas, C.R. Numerical modeling of a four-rod pumping scheme for improving TEM₀₀-mode solar laser performance. *J. Photonics Energy* **2019**, *9*, 1. [[CrossRef](#)]
23. Tibúrcio, B.D.; Liang, D.; Almeida, J.; Garcia, D.; Vistas, C.R. Dual-rod pumping concept for TEM₀₀-mode solar lasers. *Appl. Opt.* **2019**, *58*, 3438. [[CrossRef](#)]
24. Tibúrcio, B.D.; Liang, D.; Almeida, J.; Garcia, D.; Vistas, C.R.; Morais, P.J. Highly efficient side-pumped solar laser with enhanced tracking-error compensation capacity. *Opt. Commun.* **2020**, *460*, 125156. [[CrossRef](#)]
25. Liang, D.; Almeida, J.; Garcia, D.; Tibúrcio, B.D.; Guillot, E.; Vistas, C.R. Simultaneous solar laser emissions from three Nd:YAG rods within a single pump cavity. *Sol. Energy* **2020**, *199*, 192–197. [[CrossRef](#)]
26. Costa, H.; Almeida, J.; Liang, D.; Garcia, D.; Catela, M.; Tibúrcio, B.D.; Vistas, C.R. Design of a multibeam solar laser station for a megawatt solar furnace. *Opt. Eng.* **2020**, *59*, 086103. [[CrossRef](#)]
27. Almeida, J.; Liang, D.; Costa, H.; Garcia, D.; Tibúrcio, B.D.; Catela, M.; Vistas, C.R. Seven-rod pumping concept for simultaneous emission of seven TEM₀₀-mode solar laser beams. *J. Photonics Energy* **2020**, *10*, 038001. [[CrossRef](#)]
28. Costa, H.; Almeida, J.; Liang, D.; Tibúrcio, B.D.; Garcia, D.; Catela, M.; Vistas, C.R. Quasi-Gaussian Multibeam Solar Laser Station for a Megawatt Solar Furnace. *J. Sol. Energy Res. Updat.* **2021**, *8*, 11–20. [[CrossRef](#)]
29. Liang, D.; Almeida, J.; Tibúrcio, B.D.; Catela, M.; Garcia, D.; Costa, H.; Vistas, C.R. Seven-Rod Pumping Approach for the Most Efficient Production of TEM₀₀ Mode Solar Laser Power by a Fresnel Lens. *J. Sol. Energy Eng.* **2021**, *143*, 061004. [[CrossRef](#)]
30. Costa, H.; Almeida, J.; Liang, D.; Catela, M.; Garcia, D.; Tibúrcio, B.D.; Vistas, C.R. Zigzag Multirod Laser Beam Merging Approach for Brighter TEM₀₀-Mode Solar Laser Emission from a Megawatt Solar Furnace. *Energies* **2021**, *14*, 5437. [[CrossRef](#)]

31. Payziyev, S.; Makhmudov, K.; Bakhranov, S.; Sherniyozov, A.; Zikrillayev, K. Solar-Pumped Multi-Rod Laser on a Separate Heliostat of Big Solar Furnace. *Appl. Sol. Energy* **2021**, *57*, 541–551. [CrossRef]
32. Tibúrcio, B.D.; Liang, D.; Almeida, J.; Garcia, D.; Catela, M.; Costa, H.; Vistas, C.R. Enhancing TEM₀₀-Mode Solar Laser With Beam Merging and Ring-Array Concentrator. *J. Sol. Energy Eng.* **2022**, *144*, 061005. [CrossRef]
33. Tibúrcio, B.D.; Liang, D.; Almeida, J.; Garcia, D.; Catela, M.; Costa, H.; Vistas, C.R. Tracking error compensation capacity measurement of a dual-rod side-pumping solar laser. *Renew. Energy* **2022**, *195*, 1253–1261. [CrossRef]
34. Liang, D.; Vistas, C.R.; Garcia, D.; Tibúrcio, B.D.; Catela, M.; Costa, H.; Guillot, E.; Almeida, J. Most efficient simultaneous solar laser emissions from three Ce:Nd:YAG rods within a single pump cavity. *Sol. Energy Mater. Sol. Cells* **2022**, *246*, 111921. [CrossRef]
35. Skouri, S.; Ben Haj Ali, A.; Bouadila, S.; Ben Salah, M.; Ben Nasrallah, S. Design and construction of sun tracking systems for solar parabolic concentrator displacement. *Renew. Sustain. Energy Rev.* **2016**, *60*, 1419–1429. [CrossRef]
36. McFee, R.H. Power collection reduction by mirror surface nonflatness and tracking error for a central receiver solar power system. *Appl. Opt.* **1975**, *14*, 1493. [CrossRef]
37. Roth, P.; Georgiev, A.; Boudinov, H. Cheap two axis sun following device. *Energy Convers. Manag.* **2005**, *46*, 1179–1192. [CrossRef]
38. Mwithiga, G.; Kigo, S.N. Performance of a solar dryer with limited sun tracking capability. *J. Food Eng.* **2006**, *74*, 247–252. [CrossRef]
39. Nsengiyumva, W.; Chen, S.G.; Hu, L.; Chen, X. Recent advancements and challenges in Solar Tracking Systems (STS): A review. *Renew. Sustain. Energy Rev.* **2018**, *81*, 250–279. [CrossRef]
40. Kalogirou, S.A. *Solar Energy Engineering*, 2nd ed.; Elsevier: Amsterdam, The Netherlands, 2014; ISBN 9780123972705.
41. Bernardes, P.H.; Liang, D. Solid-state laser pumping by light guides. *Appl. Opt.* **2006**, *45*, 3811. [CrossRef]
42. *ASTM G173-03(2012)*; Standard Tables for Reference Solar Spectral Irradiances: Direct Normal and Hemispherical on 37° Tilted Surface. ASTM: West Conshohocken, PA, USA, 2012.
43. Prah, S. Nd:YAG—Nd:Y3Al5O12. Available online: <https://omlc.org/spectra/lasermedia/html/052.html> (accessed on 7 June 2022).
44. Hwang, I.H.; Lee, J.H. Efficiency and threshold pump intensity of CW solar-pumped solid-state lasers. *IEEE J. Quantum Electron.* **1991**, *27*, 2129–2134. [CrossRef]
45. Koechner, W. *Solid-State Laser Engineering*, 5th ed.; Springer Series in Optical Sciences; Springer: Berlin/Heidelberg, Germany, 1999; ISBN 978-3-662-14221-9.
46. Almeida, J.; Liang, D.; Vistas, C.R.; Guillot, E. Highly efficient end-side-pumped Nd:YAG solar laser by a heliostat–parabolic mirror system. *Appl. Opt.* **2015**, *54*, 1970. [CrossRef]
47. Catela, M.; Liang, D.; Vistas, C.R.; Garcia, D.; Costa, H.; Tibúrcio, B.D.; Almeida, J. Highly Efficient Four-Rod Pumping Approach for the Most Stable Solar Laser Emission. *Micromachines* **2022**, *13*, 1670. [CrossRef]
48. Vistas, C.R.; Liang, D.; Almeida, J.; Tibúrcio, B.D.; Garcia, D.; Catela, M.; Costa, H.; Guillot, E. Ce:Nd:YAG side-pumped solar laser. *J. Photonics Energy* **2021**, *11*, 018001. [CrossRef]